Planès, T. *et al.* (2016). *Géotechnique* **66**, No. 4, 301–312 [http://dx.doi.org/10.1680/jgeot.14.P.268]

Time-lapse monitoring of internal erosion in earthen dams and levees using ambient seismic noise

T. PLANÈS*, M. A. MOONEY*, J. B. R. RITTGERS†, M. L. PAREKH*, M. BEHM† and R. SNIEDER†

Earthen dams and levees are prone to progressive failure through internal erosion of their structure. Internal erosion is often invisible to current methods of inspection until it manifests itself at the exterior surface. This study focuses on the novel use of passive seismic interferometry to monitor temporal changes in earthen embankments caused by internal erosion. This technique uses the ambient seismic noise – i.e. ambient vibrations – propagating through the structure. Laboratory-scale and field-scale embankment failure experiments are monitored. Seismic impulse responses are reconstructed from the ambient noise and temporal variations in seismic wave velocities are observed throughout each test. The application of seismic interferometry on a canal embankment tested to failure by internal erosion revealed up to 20% reductions in surface wave velocity as internal erosion progressed. The monitoring of a field embankment loaded to partial failure revealed a 30% reduction in averaged surface wave velocity. Some local velocity variations showed good agreement with local pore water pressure responses.

KEYWORDS: dams; embankments; erosion; geophysics; monitoring

INTRODUCTION

In the USA alone, about 160 000 km of earth levees and 85 000 dams provide flood protection, clean water supply and renewable energy for millions of people (ASCE, 2013). This number is significantly larger worldwide. Earth dams and levees (EDLs) are prone to failure in the form of internal erosion of soils within or below the structure. This progressive failure mechanism initiates in areas of elevated gradient and weakness in EDLs soils due to inferior construction or aging. It is often invisible to current methods of inspection until it manifests itself at the exterior surface (Fell *et al.*, 2003).

Internal erosion is induced by concentrated seepage that transports soil particles through the embankment (through seepage) or its foundation (under seepage). Of particular concern, the backward erosion mechanism initiates when cohesionless particles are subject to strong seepage pressures at the downstream toe of the embankment. Soil particles are expelled upward in the form of sand boils, and the process back-propagates until a continuous path or pipe reaches the upstream reservoir or river (Van Beek *et al.*, 2010). Sometimes, sand boils appear on performing structures that do not present any immediate danger. Other times, sand boils appear only a few hours before complete failure (Foster *et al.*, 2000). Thus the presence of sand boils alone cannot be considered as a reliable early warning indicator (Kanning *et al.*, 2008).

There is a critical need to develop non-invasive techniques that can identify internal weakness or damage in EDLs during early stages to provide additional warning time and when intervention can prevent catastrophic damage and cost. If such techniques could be implemented broadly and continuously, they would enable the EDL community to carry out structural health monitoring of the tens of thousands of kilometres of EDLs within the USA and globally.

In the past decade, a passive seismic monitoring method referred to as ambient noise correlation has gained interest and experienced significant growth in both academic research and industry applications. This method reconstructs the seismic impulse response – revealing the P, S and surface wave velocities – of the subsurface between two sensors, using only the ambient noise/vibrations measured by the two sensors. It does not rely on the use of an active source, and allows continuous monitoring of the instrumented structure. Ambient noise correlation can be regarded as a particular approach within the wider field of seismic interferometry, which refers to the synthesis of a new wavefield from the correlation of other wavefields (Galetti & Curtis, 2012).

Seismic interferometry has been used to monitor or image a wide range of natural structures including oil and gas reservoirs (Bakulin *et al.*, 2007), volcanoes (Sens-Schönfelder & Wegler, 2006; Brenguier *et al.*, 2008b; Obermann *et al.*, 2013), fault zones (Wegler & Sens-Schöonfelder, 2007; Brenguier *et al.*, 2008a) and the deep earth (Boué *et al.*, 2013; Lin *et al.*, 2013). More recently, a few applications have concerned civil and geotechnical structures, including buildings (Snieder & Safak, 2006; Nakata *et al.*, 2013; Ebrahimian *et al.*, 2014; Nakata & Snieder, 2014) and landslide monitoring (Renalier *et al.*, 2010; Mainsant *et al.*, 2012). To the present authors' knowledge, no studies have addressed the topic of EDLs monitoring. In this work, seismic interferometry is used to monitor temporal changes in earthen embankments that experience internal erosion. This is done through the analysis of two datasets acquired during laboratory-scale and field-scale experiments.

In 'Background', the principles of impulse response extraction through ambient noise correlation are reviewed. The use of reconstructed responses to monitor velocity changes in the medium is then detailed. These changes reflect variations of elastic moduli and density of the material, themselves related to variations of effective stress and porosity. In 'Canal

Manuscript received 30 December 2014; revised manuscript accepted 15 October 2015. Published online ahead of print 4 December 2015.
Discussion on this paper closes on 1 September 2016, for further details see p. ii.
* Department of Civil and Environmental Engineering, Colorado School of Mines, Golden, CO, USA.
† Department of Geophysics, Colorado School of Mines, Golden, CO, USA.

embankment failure: a laboratory-scale experiment', these techniques are applied to a laboratory experiment of a canal embankment failure, and in 'IJkdijk: a field-scale experiment', they are applied to the field-scale test of a levee subject to internal erosion initiation.

BACKGROUND

Impulse response reconstruction

Seismic interferometry through ambient noise correlation is a passive method used to reconstruct the seismic impulse response – also called the Green's function – between two sensors. The Green's function is the wavefield recorded over time at one sensor when an impulsive source is triggered at the other sensor. From the impulse response, one can extract the velocity of the different seismic phases (P, S and surface waves), which are related to the density and elastic moduli of the medium. Low-strain elastic moduli themselves are related to porosity and effective stress. Ambient seismic noise can be generated by a variety of natural or human-induced sources whose frequency content span over several orders of magnitude: ≈ 1 mHz for earth free oscillations, $\approx 0{\cdot}1$ Hz for the ocean swell, ≈ 1 Hz for earthquakes, ≈ 10 Hz for road traffic.

To reconstruct the seismic impulse response from the ambient seismic noise recorded at two sensors, mathematical operations based on cross-correlation can be applied. Consider $n_A(t)$ the ambient seismic noise recorded at sensor A and $n_B(t)$ the ambient seismic noise recorded at sensor B over the same time period. In the frequency domain ω, the cross-correlation function (CRF), deconvolution function (DCF) and cross-coherence function (CHF) are defined as

$$\mathrm{CRF}_{AB}(\omega) = n_A^*(\omega) n_B(\omega) \tag{1}$$

$$\mathrm{DCF}_{AB}(\omega) = \frac{n_B(\omega)}{n_A(\omega)} = \frac{n_A^*(\omega) n_B(\omega)}{|n_A(\omega)|^2} \tag{2}$$

$$\mathrm{CHF}_{AB}(\omega) = \frac{n_A^*(\omega) n_B(\omega)}{|n_A(\omega)||n_B(\omega)|} \tag{3}$$

In each case, the product appearing in the numerator in the frequency domain corresponds to a cross-correlation in the time domain; the star notation designates the complex conjugate operation. Sensor A, chosen as the reference sensor, is called the virtual source (Bakulin & Calvert, 2006). The reconstructed DCF, CHF or CRF simulates the wavefield that would be recorded in B if an active source was triggered in A. The DCF and CHF often give cleaner responses than the bare CRF, as they include spectral whitening of the recorded ambient noise. The time-domain deconvolution $\mathrm{DCF}_{AB}(t)$ and cross-coherence functions $\mathrm{CHF}_{AB}(t)$ are obtained from an inverse Fourier transform and constitute the impulse response or Green's function between A and B.

The quality of the reconstructed response depends on the noise sources' spatial distribution and frequency content. In the ideal case of uniformly distributed and uncorrelated sources of white noise, the CHF would be closely related to the Green's function between A and B – that is, the seismic response that would be recorded in B if a Dirac type impulsive source was triggered in A at $t = 0$. The CHF would comprise the impulse response from A to B at positive times – called the causal response – as well as the impulse response from B to A at negative times – called the anticausal response. This is illustrated in Fig. 1(a) for two-dimensional (2D) wave propagation. The causal and anticausal responses

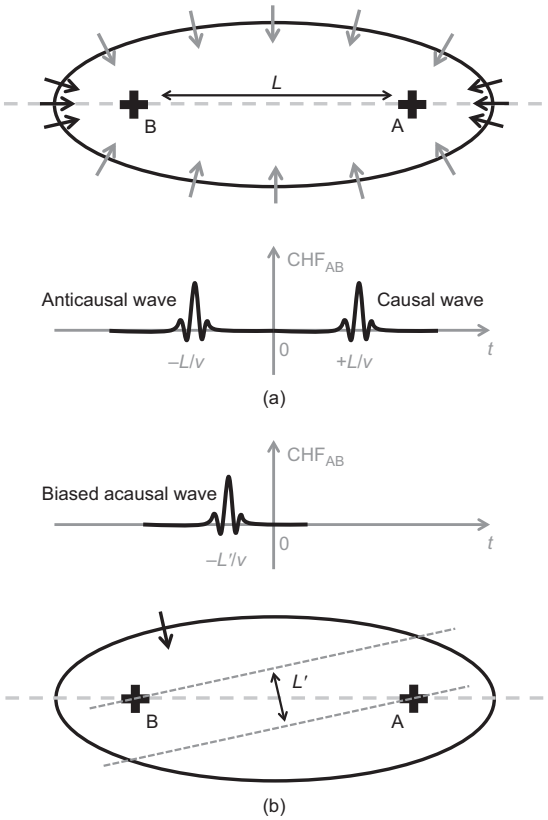

Fig. 1. (a) Schematic representation of a 2D noise source distribution around sensor A and B and the cross-coherence function CHF_{AB}. The noise events coming from directions unaligned with the sensor line (grey arrows) interfere destructively with each other and do not contribute to the CHF. The noise events coming from directions aligned or nearly aligned with the sensor line (black arrows) interfere constructively and contribute to CHF_{AB}. The causal (resp. anticausal) wavelet, generated by ambient noise coming from the right (resp. left) shows a travel time of $+L/v$ (resp. $-L/v$), L being the distance travelled between the sensors and v the wavelet velocity. (b) Noise from a single direction (black arrow) and associated CHF_{AB} showing a biased impulse response. The acausal wavelet shows a travel time of $-L'/v$, L' being the effective distance travelled by the noise events between detections by the sensors. In this case, the use of travel time and distance L to estimate the velocity v would be incorrect

are symmetric with respect to time zero, and are generated by noise sources located on the side of sensor A and on the side of sensor B, respectively (black arrows). They travel a distance $L = \|\mathrm{AB}\|$ and probe the medium between the sensors. Because of their uniform repartition, the noise events coming from directions unaligned with the sensor line (grey arrows) interfere destructively and do not contribute to the CHF.

In the case of non-uniform distribution of noise sources, the reconstructed responses can differ dramatically from the true impulse response. The case of a single incoming noise source direction is illustrated in Fig. 1(b). The reconstructed response shows a single acausal wavelet, whose travel time corresponds to a shorter effective path L'. In this case, the region probed by this wavelet can be located away from the inter-sensor region.

Surface waves are the easiest mode to reconstruct from ambient noise (Snieder & Larose, 2013). With their propagation being confined to the surface, a lot of possible locations for noise sources can contribute to a constructive interference in the cross-correlation process. On the contrary, the reconstruction of body (P and S) waves is much more difficult, as constructive noise source locations are very scarce (Forghani & Snieder, 2010). The wavelength of the

reconstructed waves – and thus the spatial resolution of any subsequent processing – is constrained by the frequency content of the ambient noise and the wave propagation velocity of the studied medium. In the experiments presented in the following, the studied wavelengths are of the order of a few metres. To improve the quality of the reconstructed signals, several pre-processing and post-processing steps can also be applied (Bensen *et al.*, 2007; Behm *et al.*, 2014).

Time-lapse velocity monitoring

By reconstructing the CHFs between different pairs of sensors and at different time intervals, it is possible to monitor changes in a medium over elapsed time. The temporal evolution of wave velocity can be analysed by comparing the arrival time of a specific seismic phase in the CHFs at two different times. Here $\mathrm{CHF}^1_{\mathrm{AB}}$ (resp. $\mathrm{CHF}^2_{\mathrm{AB}}$) is the CHF between A and B at time 1 (resp. time 2). The temporal delay δt of the arrival at time 2 compared to arrival at time 1 can be measured using cross-correlation

$$\mathrm{CC}(\tau) = \frac{\int_{\Delta t} \mathrm{CHF}^1_{\mathrm{AB}}(t')\mathrm{CHF}^2_{\mathrm{AB}}(t'+\tau)\mathrm{d}t'}{\sqrt{\int_{\Delta t} \mathrm{CHF}^1_{\mathrm{AB}}(t')^2\mathrm{d}t' \int_{\Delta t} \mathrm{CHF}^2_{\mathrm{AB}}(t')^2\mathrm{d}t'}} \quad (4)$$

where Δt is a time window that encompasses the seismic wavelet of interest. The actual time delay δt is the value of τ for which the normalised cross-correlation CC reaches its maximum value $\mathrm{CC}_{\max}$. Let t_c be the centre of the time window Δt. The relative velocity change between times 1 and 2 is obtained by

$$\frac{\mathrm{d}v}{v} = -\frac{\delta t}{t_c} \quad (5)$$

Wave velocity changes reflect changes in soil properties, namely bulk modulus, shear modulus and density. These parameters are themselves affected by the effective stress and the void ratio/porosity of the soil. The relationships between low-strain elastic moduli, void ratio and effective confining stress state are well established across soil types (Ishihara, 1996; Santamarina *et al.*, 2001). In sands, for instance, the low-strain shear modulus G_0 has the following general empirical relation

$$G_0 = AF(e)\sigma'^n_0$$

$$F(e) = \frac{2{\cdot}17 - e^2}{1+e} \quad (6)$$

where e is the void ratio, σ'_0 is the effective mean confining stress, and A and n constants that are dependent on the soil. The function $F(e)$ decreases with increasing void ratio (up to $e \approx 2$).

The S-wave velocity is defined as $v_s = (G_0/\rho)^{1/2}$, with ρ the density of the soil. A reduction in S-wave velocity thus results from an increase in void ratio (or porosity) and/or a decrease in effective confining stress. Internal erosion involves an increase in void ratio within the area of concentrated seepage as particles are washed away. The resulting localised stiffness reduction induces effective stress redistribution by way of arching.

CANAL EMBANKMENT FAILURE: A LABORATORY-SCALE EXPERIMENT

Experimental set-up

A scaled canal embankment model was constructed and tested to failure by internal erosion in an indoor laboratory by the US Bureau of Reclamation in Denver, Colorado. This model was part of a series of tests designed to study the breach processes of typical irrigation canal embankments, considering various material properties and failure initiation conditions (Wahl & Lentz, 2012).

The test facility consists of a 21·3 m long trapezoidal canal constructed between two headboxes – upstream and downstream – for supply and recovery of water (Fig. 2). The canal is formed by non-erodible plywood walls, except for a 6·10 m long section where one sidewall is replaced by a compacted silty-sand embankment (Wahl & Lentz, 2012). The embankment was constructed of low-plasticity (plasticity index, PI = 6) silty sand (Unified Soil Classification System (USCS) designation SM) including 15% clay, 20% silt and 64% sand (coefficient of uniformity $C_u = 94$). The soil was placed and compacted 0·5% dry of standard Proctor optimum moisture. The lower 30 cm was compacted to 98% of maximum dry

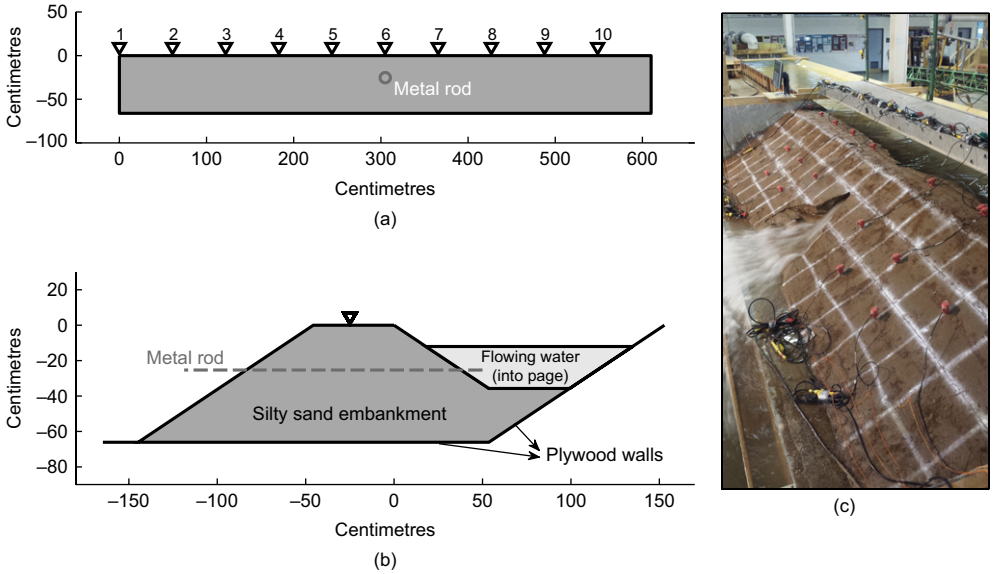

Fig. 2. (a) Schematic front view and (b) cross-sectional view of the canal embankment. A 1·3 cm diameter metal rod was embedded in the middle of the structure during construction, 25 cm below the crest. Ten vertical component geophones were deployed on the crest, with a 61 cm spacing. (c) Photograph of the embankment and flowing breach, 5 h after the piping initiation

density and the upper 36 cm was compacted to 87% of maximum dry density.

The crest of the embankment lies 66 cm above the landside toe and 36 cm above the canal invert (see Fig. 2). During construction, a 1·3 cm diameter metal rod was placed through the embankment, extending from its waterside to its landside face and 25 cm below the crest. After the establishment of a steady flow between the two headboxes, the experiment began with the manual pulling of the metal rod to initiate a piping process ($T = 0$). The water slowly eroded this artificially created pipe, reaching the crest of the embankment after 6·5 h. The test was stopped 30 min after this full breach, as the pumps were no longer able to maintain adequate flow. The piping water was collected in a recovery basin located next to the landside toe and the flow was measured with two methods. During the first 2·5 h, the flow was measured with a magnetic flow meter. After this, the flow was too significant for the device and could only be measured by differencing the inflow/outflow from the supply and recovery headboxes. The time lapse evolution of the piping flow and snapshots of the breach are presented in Fig. 3.

To passively monitor the structure, ten vertical component geophones were deployed on the crest of the embankment, with 61 cm spacing between geophones (Fig. 2). These geophones have a 20–400 Hz bandpass. The ambient noise was recorded semi-continuously throughout the test using a Geometrics Geode seismograph at a 2 kHz sampling frequency. These records are stored in 30 s-long files separated by 8 s-long breaks (a limitation of the DAQ system).The sources of ambient noise in this test are not specifically identified, but are assumed to be related to the high machine activity in the facility.

Impulse response reconstruction

For each 30 s recording period, the signals are first filtered around different centre frequencies with 50% relative bandwidths. The signals are then normalised in the time domain by discarding the amplitude and keeping only the sign (1 bit normalisation). This gives more weight to continuous background noise sources compared to transient parasite noise sources. In each frequency band, the deconvolution function (DCF) between each pair of sensors is then calculated according to equation (2). The normalised reconstructed responses along the crest are presented as correlogram panels – that is, panels of seismograms reconstructed through cross-correlations – in Fig. 4. In this figure, sensor 1 has been chosen as the virtual source, meaning that the signals recorded at individual sensors 2–10 are cross-correlated with the signal recorded at sensor 1. The DCFs have been stacked for a period of 20 min within the first hour of the experiment to improve their signal-to-noise ratio.

In the 30 Hz-centered frequency band, both the causal – left to right wave propagation – and anticausal – right to left wave propagation – branches are observed. The symmetry of the two branches suggests that the noise is sourced from both the left side and right side of the embankment in this frequency range. The apparent group velocity of the causal wave – $v \approx 100$ m/s – is estimated with manual picking of the wavelet maxima, and a linear regression (solid line). The mirror image of the solid line is represented as a dashed line over the anticausal branch.

Through the analysis of an active baseline hammer shot performed at the beginning of the experiment, the true group velocity has been estimated to be $v \approx 85$ m/s in this frequency band. The apparent velocity being slightly larger means that the noise sources are probably located slightly off the sensor line, leading to a shorter effective travelled distance. Interestingly, only the causal branch is observed in the higher frequency bands. This could mean that the high-frequency noise propagating from right to left in the structure is significantly attenuated before reaching sensor 1 (the virtual source). Indeed, in the high-frequency bands, greater attenuation is indicated by the quick degradation of signal-to-noise ratio with respect to travelled distance.

In each of these frequency bands, the wavelengths of the reconstructed waves range from approximately 1 m to 3 m. This corresponds to the width and height of the embankment in this test. In addition, as the vertical motion is recorded, it is assumed that the reconstructed waves are shear type guided waves rather than surface waves. This means that the waves are propagating along a one-dimensional (1D) effective structure, probing the whole cross-section of the embankment along their way. In contrast, surface waves only sense a limited depth of material below the surface and are not influenced by material or boundaries beyond this depth. An estimation of the vertical profile of shear waves' velocity from surface wave dispersion analysis is therefore not applicable here. This is a result of the laboratory scale of this experiment. A field-scale experiment with similar ambient noise frequency content would not suffer this limitation, given the scale of embankments.

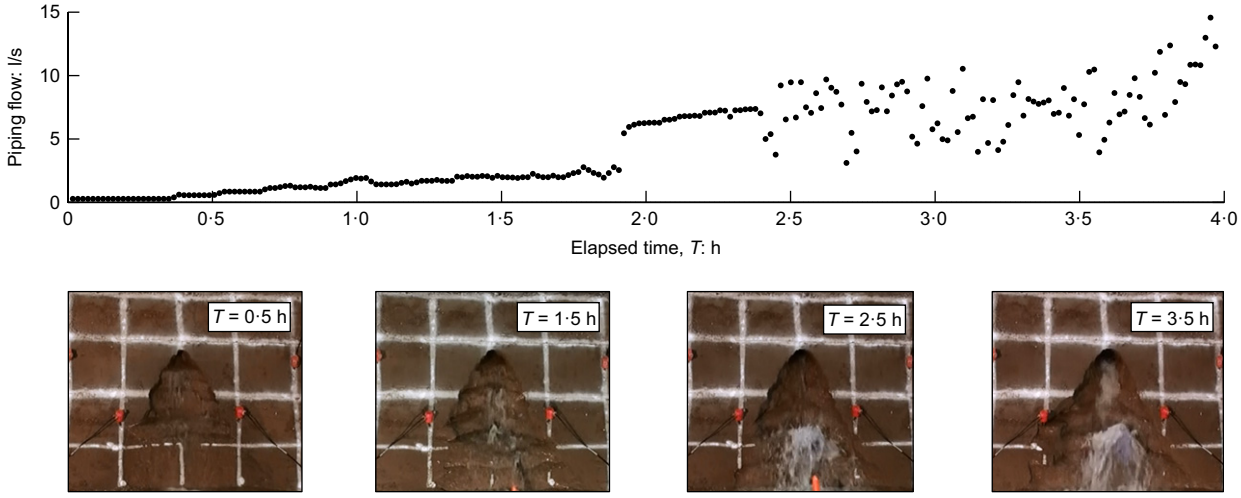

Fig. 3. Piping flow during the first 4 h of the experiment. The flow is measured by a magnetic flow meter until 2·4 h and is then estimated by differencing the inflow and outflow from the supply/recovery headboxes. Snapshots of the breach are presented for $T = 0{\cdot}5$, 1·5, 2·5 and 3·5 h. The grid spacing is 30 cm

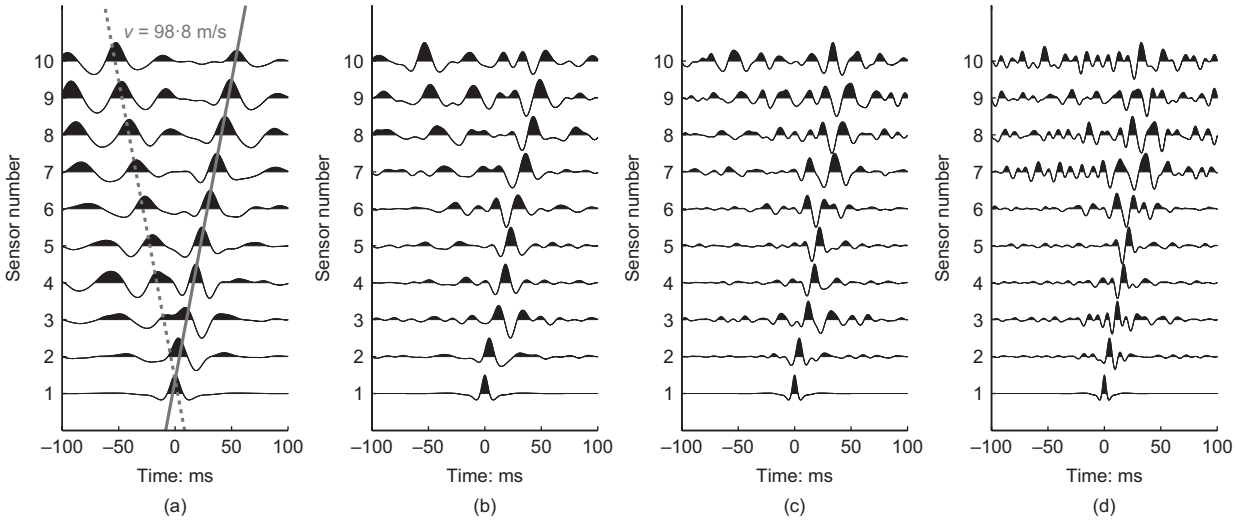

Fig. 4. Correlograms obtained from 20 min of noise recorded on the crest of the embankment during the first hour of the experiment (low piping flow). Sensor 1 is chosen as the virtual source. In the (a) 30 Hz-centred and (b) 50 Hz-centred frequency bands, both the causal – left to right wave propagation – and anticausal – right to left wave propagation – branches are observed. In the (c) 70 Hz-centred and (d) 90 Hz-centred frequency bands, only the causal branch is observed and higher signal attenuation is noticed

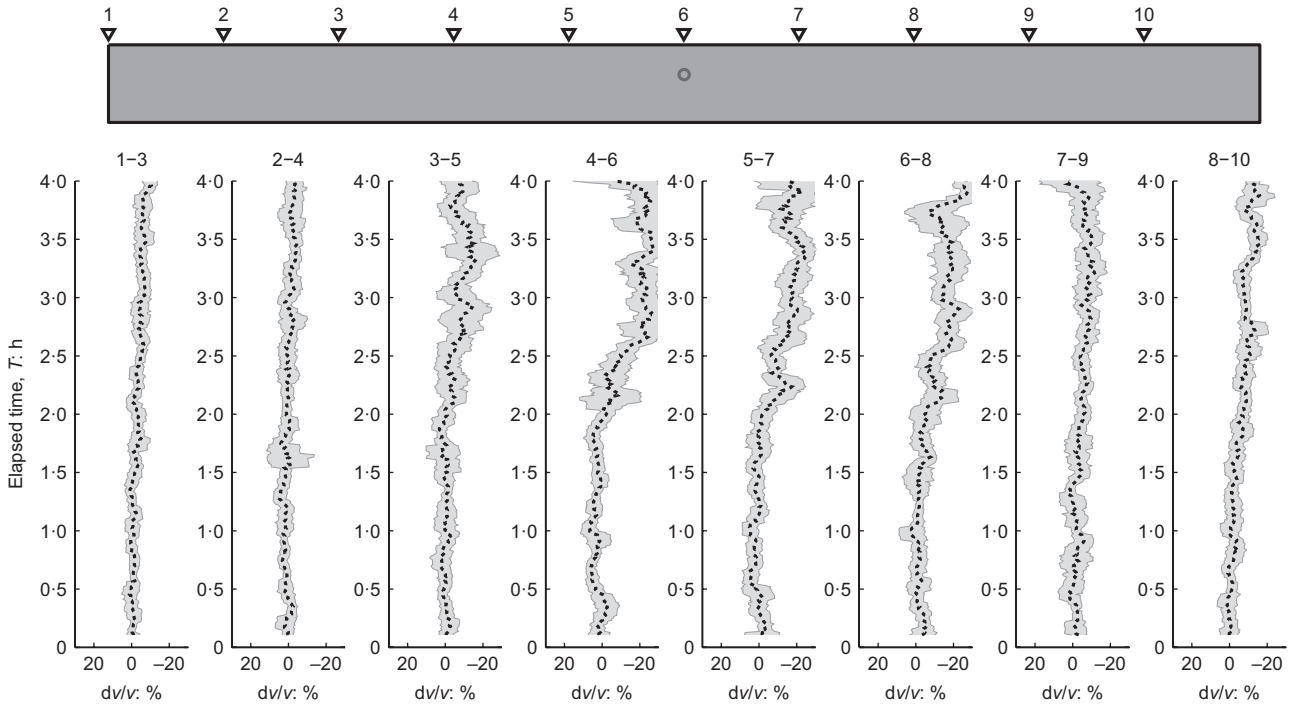

Fig. 5. Relative velocity changes for the 1·2 m offset sensor pairs, along the first 4 h of the experiment. The largest velocity drop (≈ 20%) is observed around the centre of the structure, where the piping process is expected to induce strong stress redistributions

Temporal monitoring

To monitor the wave velocity with elapsed time, the 50 Hz-centred frequency band is chosen as a trade-off between spatial resolution and stability/coherence of the waveforms to provide stable measurements. For each pair of sensors, a reference DCF is first computed by stacking about 10 min of DCFs from elapsed time 15 min to 25 min of the experiment, during the early limited pipe flow. At each elapsed time of the experiment, the current DCFs are then compared to the reference DCFs. Velocity variations during the experiment are computed following equation (4). These variations are shown for the 1·2 m offset pairs of sensors in Fig. 5. The velocity variations can be estimated either on the causal or anticausal wavelet. In practice, the one that has the best signal-to-noise ratio is selected. In this figure, the causal wavelet is selected for pairs 1–3 to 6–8, and the anticausal wavelet is selected for pairs 7–9 and 8–10. Fig. 5 data reflect the first 4 h of the experiment, where significant piping erosion progresses (Fig. 3). After these 4 h, the structure becomes too damaged and the interferometry fails to produce stable results, that is, the waveform coherence decreases dramatically.

Sensors pairs 4–6, 5–7 and 6–8 show the strongest velocity drops, starting around $T = 2$ h and decreasing about 20%. The other sensor pairs show a smaller and more continuous velocity decrease of about 10%. These measurements are in agreement with the physical location of the pipe that is expected to influence much more the centre of the structure than its sides. Given the wavelengths involved (≈ 2 m), the

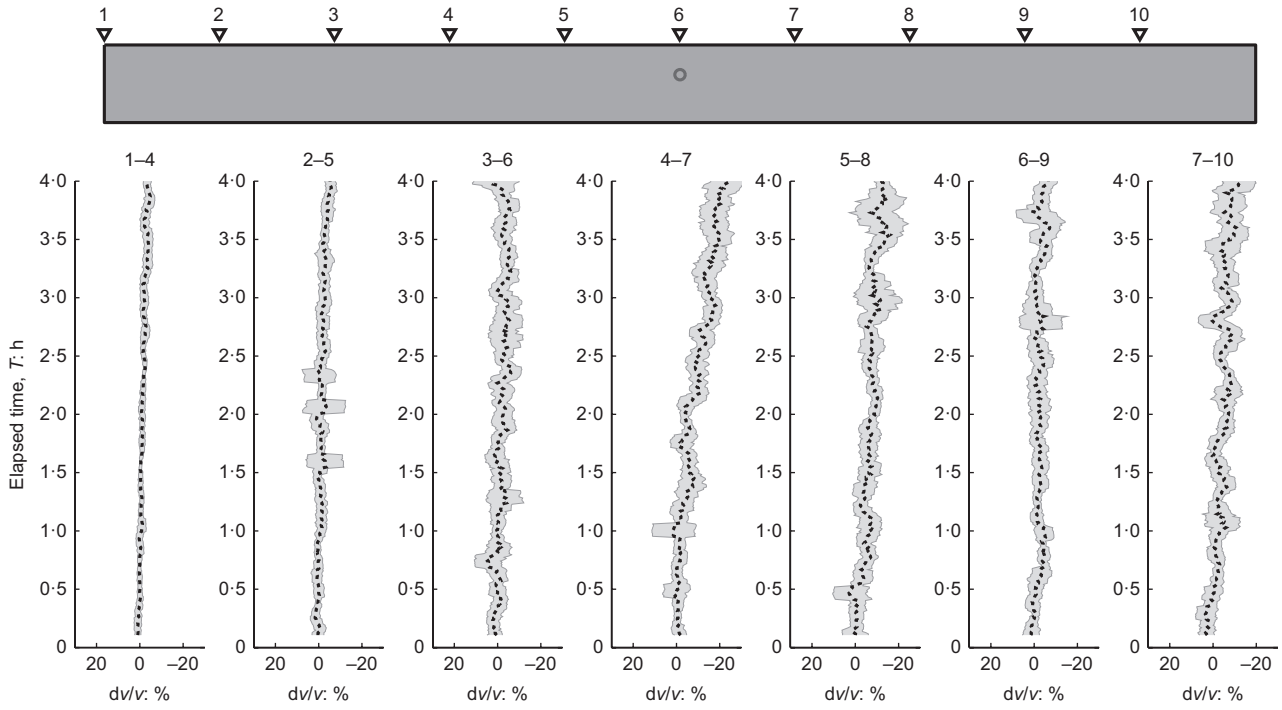

Fig. 6. Relative velocity changes for the 1·8 m offset sensor pairs, along the first 4 h of the experiment. The largest velocity drop (≈ 20%) is observed around the centre of the structure, where the piping process is expected to induce strong stress redistributions

precise location or geometry of the pipe cannot be retrieved, and the initial slowly increasing piping flow ($T = 0{\cdot}5$–2 h) is not captured. The observed velocity drop is assumed to result from a structure modification in a larger area around the pipe, most likely due to stress redistribution. This larger structural change is captured from $T = 2$ h, and this time corresponds to the steep increase of measured piping flow (see Fig. 3).The velocity variations for the 1·8 m offset pairs of sensors are presented in Fig. 6. Similar behaviours are observed, with a larger spatial averaging effect due to the larger sensor spacing.

These observations demonstrate the feasibility of passively monitoring temporal changes taking place in the embankment. In addition, the lateral dependence of these observations shows the possibility of spatial mapping of the failure-prone area. Owing to reasons beyond the authors' control, it was not possible to collect ambient vibration data before the initiation of the piping. Thus in this experiment, because the reference state is already experiencing internal erosion, only the progression and not the onset of the erosion could be monitored.

Analysis of signal attenuation

In a homogeneous medium, the amplitude of a propagating wave decreases with travel distance due to geometrical spreading and intrinsic absorption (material damping). As discussed in 'Impulse response reconstruction', it is assumed that the waves reconstructed here are shear type guided waves propagating along a 1D effective structure (the embankment). The geometrical spreading should then be negligible and the waveform attenuation solely related to material damping. The intrinsic absorption of a material describes its capacity to dissipate the wave energy into heat. For a given frequency, it can be quantified by the attenuation length L_a that corresponds to the distance after which a wavelet has lost about 63% of its energy. More precisely, for a 1D propagation, the intensity of a wavelet decreases as

$$I(r) = I_0 e^{-(r/L_a)} \tag{7}$$

where r is the travelled distance and I_0 is the intensity at the source location. Here, the intensity of the reconstructed wave is estimated as the average of its squared amplitude in a time window that encompasses the wavelet. This intensity is estimated for all travelled distances and for each of the frequency bands. In Fig. 7, the logarithms of the intensities are plotted against travelled distances, for the 50 Hz-centred (Fig. 7(a)), 70 Hz-centred (Fig. 7(b)) and 90 Hz-centred (Fig. 7(c)) frequency bands. The attenuation lengths are estimated from the slope α of the linear regressions as $L_a = -1/\alpha$. As expected, the higher the frequency is, the smaller is the attenuation length. The attenuation length is plotted against the central wavelength λ (Fig. 7(d)) and shows linear behaviour. From another linear regression, the material damping ratio $D = 0{\cdot}076$ is estimated according to

$$L_a = \frac{\lambda}{4\pi D} \tag{8}$$

It is related to the material quality factor $Q = 1/(2D) \approx 6{\cdot}6$. The damping ratio $D = 0{\cdot}076$ found here is in the expected range of the silty sand embankment soil under seismic strains (Ishihara, 1996). The damping ratio is influenced by several of the soil properties and its passive time-lapse analysis could thus be used as a complementary technique to monitor erosion-related changes in embankments. This analysis is, however, beyond the scope of the present study.

IJKDIJK: A FIELD-SCALE EXPERIMENT

The IJkdijk (pronounced 'ike dyke' and Dutch for 'calibration levee') is a field facility in the Netherlands where full-scale levees have been constructed and loaded since 2007. The goals of the IJkdijk programme are to improve understanding and prediction of failure/collapse mechanisms, the testing of new inspection techniques, sensor systems and technologies for mitigation (Flood Control IJkdijk, 2015). During the September 2012 test, multiple geophysical surveys were performed, including seismic and acoustic emissions, electrical resistivity, self-potential and

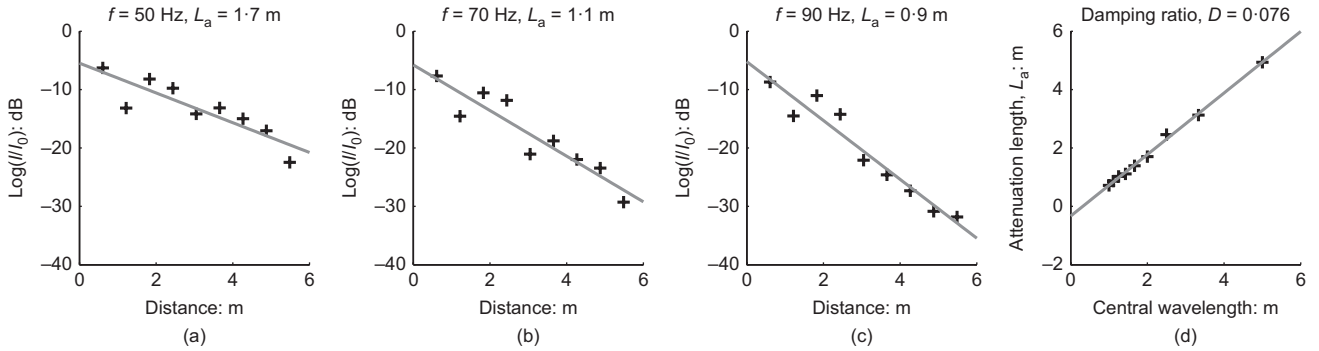

Fig. 7. Estimation of the attenuation length L_a in the (a) 50 Hz-centred, (b) 70 Hz-centred and (c) 90 Hz-centred frequency bands. A linear regression of the logarithm of the wavelet intensity plotted against travelled distance gives $L_a = 1{\cdot}7$, $1{\cdot}1$ and $0{\cdot}9$ m in the respective frequency bands. These attenuation lengths are plotted against central wavelength (d) and another linear regression gives an estimation of the damping ratio $D = 0{\cdot}076$

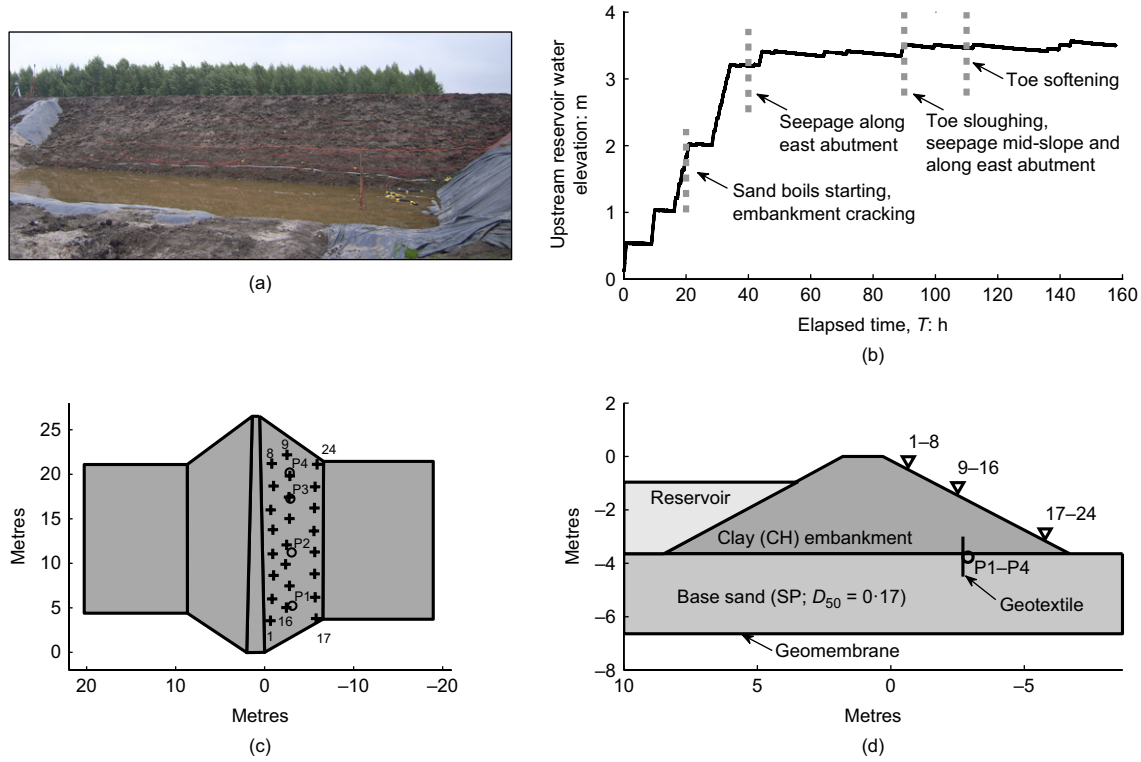

Fig. 8. (a) Downstream face, (c) schematic plan view and (d) cross-sectional view (d) of the IJkdijk. The 24 geophones are spread out along three lines on the downstream face (c). The loading schedule and main visual observations are also presented (b)

terrestrial Lidar (Mooney *et al.*, 2014; Rittgers *et al.*, 2014). The work presented here focuses on the analysis of the passive seismic data.

Experimental set-up

The structure consists of a 28 m long and 4 m tall high-plasticity clay (PI = 50–60) embankment constructed in two compacted lifts over a 3 m thick foundation of poorly graded fine sand (USCS designation SP; $D_{50} = 0{\cdot}17$ mm, $C_u = 1{\cdot}7$) (see Fig. 8). The sand basin was constructed within an impermeable geomembrane-lined basin and fully saturated, forming a hydraulically isolated upstream reservoir and a constant-head downstream reservoir with a gauged outlet system. The clay embankment soil was compacted to 90% standard Proctor max. dry density at a water content of 45–65% (plasticity limit, PL = 26–33). This levee structure is typical of those found in the Netherlands. Water seeps primarily through the underlying sand layer (underseepage). Backward propagation internal erosion (initiating at the toe) is a major concern of instability in these structures.

During the experiment, the upstream reservoir was filled with water in stages to simulate realistic hydraulic loading events. The loading schedule (see Fig. 8(b)) was carried out until a critical horizontal hydraulic gradient was established and concentrated seepage and internal erosion were initiated at the toe. Unlike the canal embankment test, the IJkdijk test did not experience full breach. A geotextile – permeable to water but not sand – was installed 4 m upstream from the toe and prevented the backward eroding channels from reaching the upstream side (Fig. 8(d)). Rather, sand boils started to occur around $T = 20$ h at the toe due to concentrated seepage and spread along the whole toe with the increase of water level. This led to some localised toe softening behaviour starting around $T = 90$ h. Upstream water elevation and pore water pressure were monitored

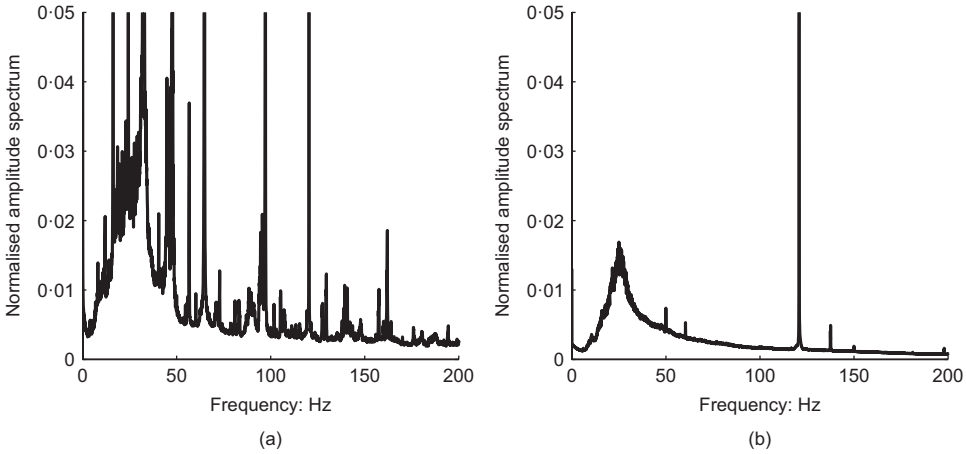

Fig. 9. Frequency content of the ambient noise, averaged (a) over a 10 min busy period and (b) over a 10 min quiet period. Most of the energy is contained in the 5–100 Hz frequency band. The observed spikes are assumed to be caused by electromagnetic and mechanical coupling of the sensors with the machines operated on site

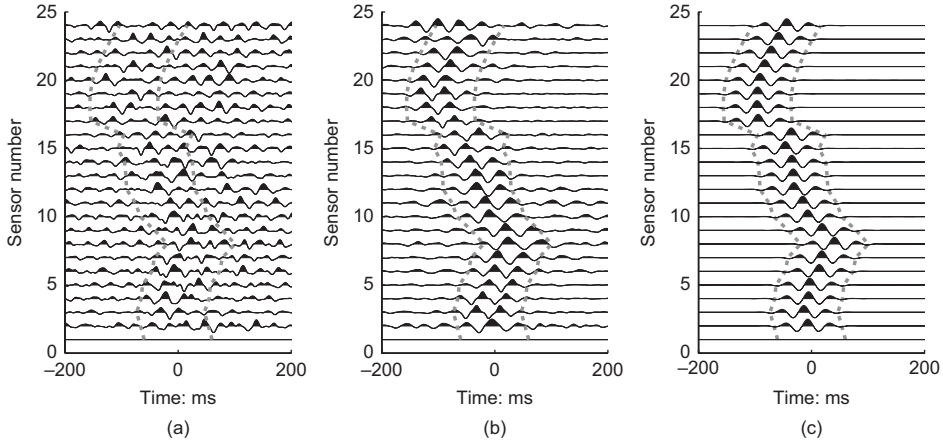

Fig. 10. Correlograms reconstructed from 10 min of ambient noise, choosing sensor 1 as the virtual source (see Fig. 8(c)): (a) during a busy period and (b) during a quiet period. (c) A synthetic correlogram constructed using the grid search algorithm and the frequency content of the noise. The synthetic wavelets are encompassed by the dashed grey lines. These lines have also been plotted on the busy and quiet period correlograms for comparison purposes

during the experiment using an array of piezometers installed in situ prior to construction.

Twenty-four vertical component geophones were deployed along three lines on the downstream face of the dam, buried between 25 cm and 75 cm below the surface to maximise the coupling with the ground and reduce noise caused by rain or wind (Fig. 8). Using a Geometrics Geode seismograph, 6 days of ambient noise were recorded semi-continuously, at a 1 kHz sampling frequency. The records are cut into 16 s-long files and separated by 3 s-long breaks due to data logging and transfer capacities of the system.

Impulse response reconstruction

The frequency content of the recorded ambient noise is presented in Fig. 9, averaged over a 10 min busy period (here shown for $T = 92$ h) and over a 10 min quiet period (here shown for $T = 118$ h). The quiet period occurred when people and equipment were minimally active and the busy period occurred when people and equipment were active on the embankment. Most of the energy is contained between 5 Hz and 100 Hz. The numerous observed spikes during the busy period are assumed to result from the electromagnetic and mechanical coupling of the sensors with the various machines operated on site. These include a man lift used for visual inspection every 1–4 h, generators, pumps and so on. Given the frequency content of the ambient noise, the raw signals are downsampled to 500 Hz in order to reduce the computing time needed in the next steps. These signals are then bandpass filtered from 5 Hz to 100 Hz. After clipping the amplitude of the signals (1-bit normalisation), the cross-coherence operation (equation (3)) is applied for each possible pair of sensors, and for each 16 s-long recorded segment. The authors' analysis showed that stacking the CHFs over 10 min of elapsed time ensured good signal stability and maintained good time resolution for monitoring purposes. Accordingly, each response corresponds to a stack of about 30 CHFs.

In Fig. 10, typical correlograms reconstructed from 10 min of noise are presented, choosing sensor 1 as the virtual source. The correlogram obtained from a busy period around $T = 92$ h does not reveal any coherent pattern, meaning that machine-dominated noise does not constructively interfere. The correlogram obtained from a quiet period around $T = 118$ h shows one set of coherent arrivals, assumed to be surface waves. The move-out pattern, showing three distinct slopes, is in qualitative agreement with the sensor layout along three lines (Fig. 8). If the noise sources were distributed uniformly around the levee, symmetrical arrivals around time zero would be observed, that is, the causal and

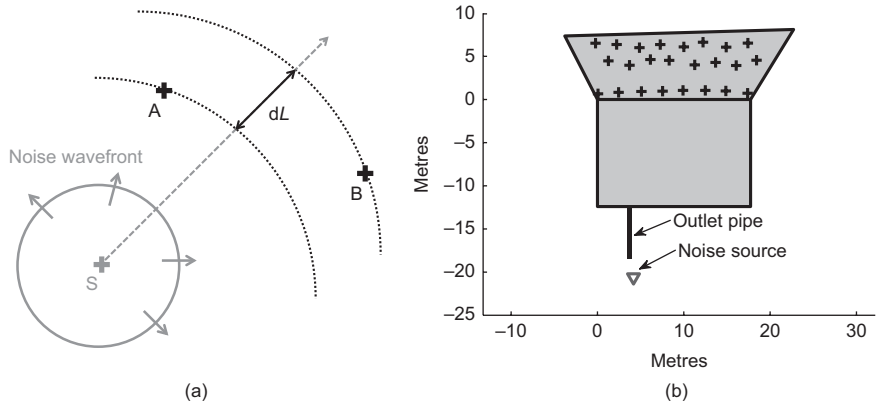

Fig. 11. (a) Schematic diagram of the effective distance dL travelled between sensors A and B by a noise wavelet emitted in S, assuming a uniform surface wave velocity over the medium. (b) Position of the geophones orthogonally projected on the downstream face of the levee (crosses). The inferred position of the noise source (triangle) is located near the exit of the outlet water pipe

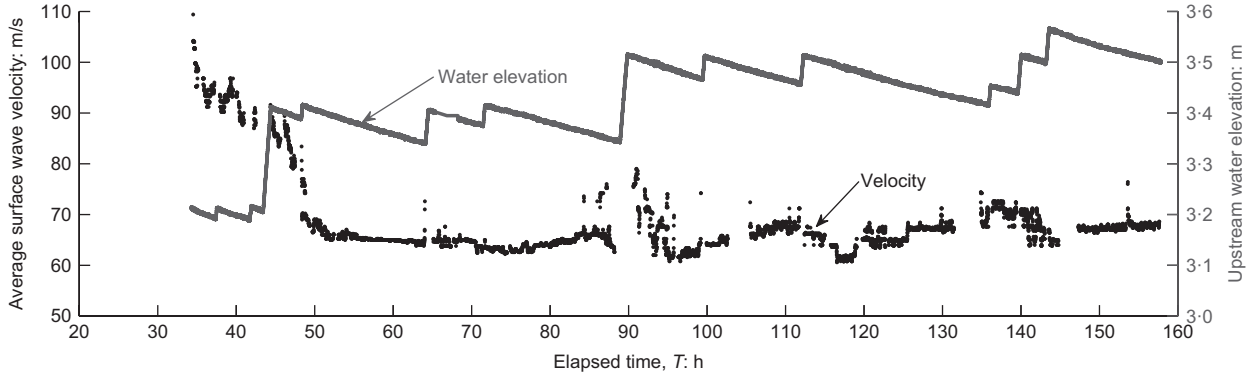

Fig. 12. Water elevation in the upstream reservoir (solid line) and average surface wave velocity (dots) along elapsed time estimated from the grid-search algorithm. A strong velocity drop from 95 to 65 m/s occurs around $T = 45$ h. The velocity then fluctuates between 60 and 70 m/s

anticausal responses (see 'Impulse response reconstruction'). Here, only one set of arrivals is observed, indicating that the noise is likely to be generated from one preferential direction or location. Because the noise sources are not uniformly distributed, the individual reconstructed impulse responses are biased and do not correspond to a straight trajectory between two sensors (see 'Impulse response reconstruction'). To interpret the observed arrival times and extract true surface wave velocities, the source position must be located.

The position of the noise source and average surface wave velocity during the 10 min quiet period used to compute the correlogram of Fig. 10(b) are estimated. Although only the subset of the responses with sensor 1 as the virtual source was displayed, the full set of impulse responses reconstructed during this period is utilised. Given a hypothetical noise source location S at the surface and a given pair of sensors at A and B, it is possible to calculate the effective distance dL travelled by a noise wavelet as $\mathrm{d}L = \|\mathrm{B} - \mathrm{S}\| - \|\mathrm{A} - \mathrm{S}\|$ (see Fig. 11(a)). Adding a hypothetical average velocity, v, the corresponding travel time $t_{\mathrm{AB}} = \mathrm{d}L/v$ between A and B can be determined. To find the velocity and noise source location that best explains the selected set of reconstructed responses, a grid search is performed over a large range of possible noise source locations and surface wave velocities. For each potential location and velocity, a corresponding wavelet arrival time is calculated for each pair of sensors. The root mean squares (RMS) of the reconstructed responses are computed in a 50 ms time window centred on these arrival times and then stacked over all pairs of sensors. Each hypothetical noise source location and surface wave velocity thus gives a single value of stacked wavelet RMS. The location and velocity that give the largest stacked RMS are those that best explain the reconstructed responses. The 2D layout of the sensors is a key condition to locate the noise source. The problem would be undetermined with a 1D sensor layout as the one presented in 'Canal embankment failure: a laboratory-scale experiment'.

The grid search algorithm operated over the selected quiet period estimates an average velocity $v = 62$ m/s and a noise source position shown in Fig. 11(b). Using this source position and average velocity, a synthetic correlogram is constructed (Fig. 10(c)) for visual confirmation. The inferred position of the noise source (Fig. 11(b)) corresponds to the location of the outlet pipe of the downstream basin, where the water flows through a short conduit and splashes into a drainage canal. This suggests that this artificial waterfall is the dominant noise source during quiet periods, that is, when machines are not operated. This ambient noise source is unique to this experiment and is likely to be different from noise sources found near other embankments. However, localised ambient noise sources of other origins could be encountered and their use for temporal monitoring is worth investigating.

Temporal monitoring

With the position of the dominant noise source known, the same analysis can be performed at different quiet times, with the average surface wave velocity remaining the only estimated parameter. Time periods involving machine operations were not used in the analysis. This comprised a small portion of the data (15 h of data over 160 h). The estimated

average surface wave velocity throughout the 160 h experiment is shown in Fig. 12. The water elevation in the upstream basin is also represented. It is noted that the first 30 h of the experiment are discarded due to lack of coherent signal. This lack of coherent signal at early elapsed time is related to the absence of consistent outlet flow. A strong velocity drop initiates around $T = 35$ h and continues even more sharply at $T = 45$ h, levelling off at $T = 50$ h. This average velocity decrease follows sand boil formation and sand production near the toe, as well as embankment cracking and upstream water elevation increase. The velocity then fluctuates from 60 to 70 m/s, with other possible correlations of velocity drops with water elevation increases around $T = 90$ h, $T = 110$ h and $T = 140$ h. Given the frequency content of the responses and the estimated velocity of the surface waves, the central wavelength is about 3–4 m. The velocity changes probed by the surface waves are therefore interpreted as a spatial average of changes possibly taking place in the clay embankment as well as in the sand foundation.

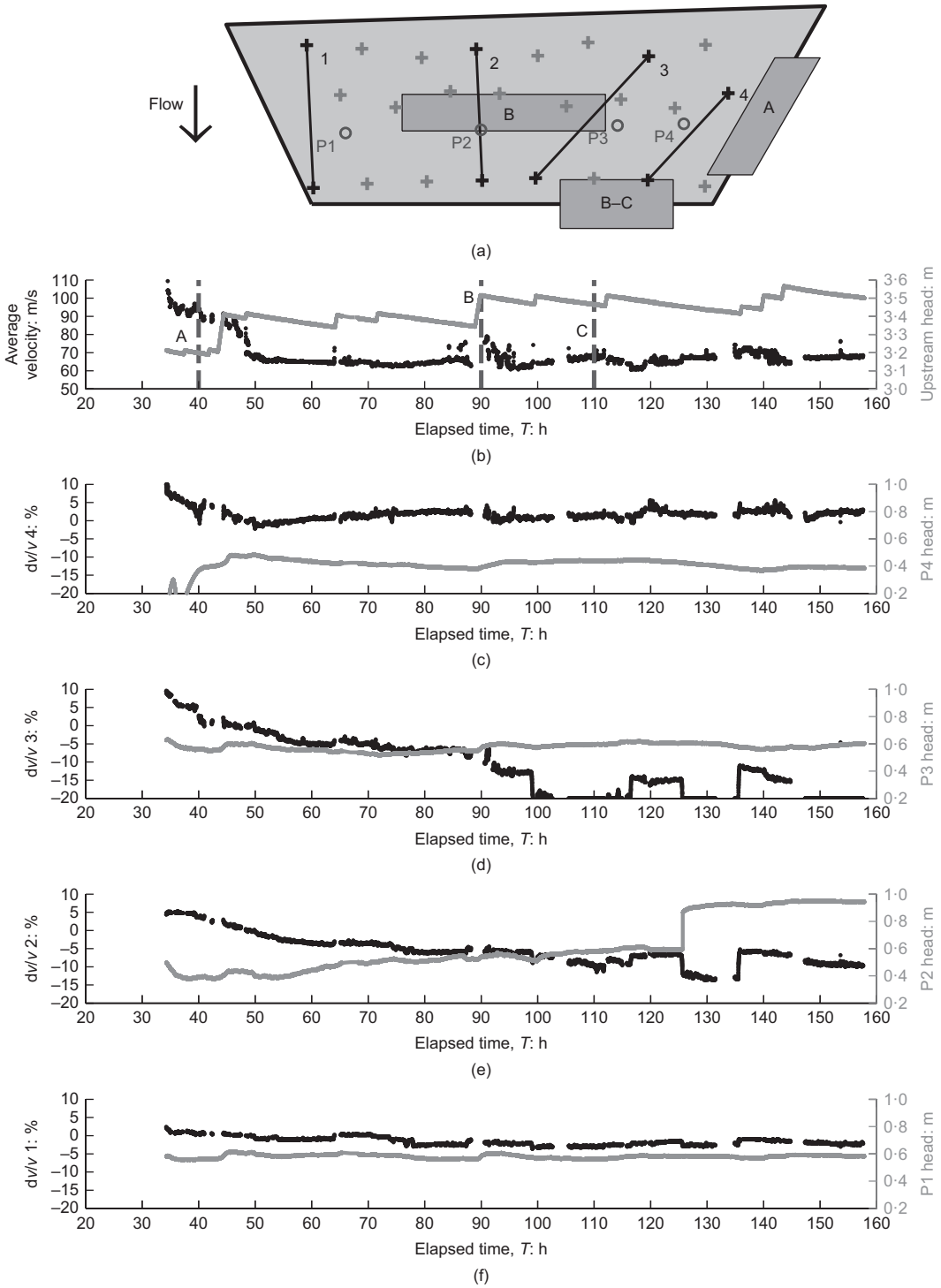

Fig. 13. (a) Schematic diagram of selected sensor pairs (1–4) and piezometers (P1–P4) projected on the downstream face of the dam. Three areas of visually observed seepage (A on abutment and B midslope) and toe softening/sloughing (B and C) are also represented. Parts (c) to (f) show the relative velocity changes estimated with the individual pairs along with the pore water pressure measured by the piezometers. (b) The water elevation in the upstream reservoir and average surface wave velocity from Fig. 12 are also presented for comparison

A few sensor pairs are selected to explore the spatial distribution of the occurring changes. These sensor pairs are chosen so that they are approximately aligned with the noise source location. This ensures that there is coherent seismic noise propagating between receivers to image the medium. For each of these selected pairs, a reference impulse response is constructed by stacking 1 h worth of CHFs around elapsed time $T = 50$ h, a time when the stability of the responses improves significantly. Similar to the canal embankment analysis, the velocity variations on these individual pairs are computed according to equation (4) throughout the elapsed time of the experiment. The estimated relative velocity changes are presented in Fig. 13, along with the time lapse evolution of the pore water pressure measured by various embedded piezometers.

Relatively small velocity variations are observed across sensor pairs 1 and 4, located on the ends of the levee. This is consistent with all other data from the experiment; that is, pore water pressure was constant (Fig. 13) and there were no local observations of internal erosion in these areas (Mooney *et al.*, 2014). Sensor pair 2 shows a gradual decrease in local surface wave velocity from $T = 35$ h to $T = 110$ h that is consistent with the gradual increase in local pore water pressure response and consequent decrease in local effective stress. Sensor pair 2 also exhibits a steep velocity drop around 125 h, coincident with a sharp pore water pressure increase measured by piezometer 2. It is difficult to pinpoint the exact physical cause of this behaviour; however, a liquefaction zone shown as B–C in Fig. 13 emerged during this general time. Sensor pair 3 shows two steep velocity drops around 99 h and 125 h, followed by steep recoveries around 116 h and 135 h respectively. The first steep drop is coincident with a small water elevation increase in the upstream reservoir and correlates with measurements of self-potential anomalies. These self-potential anomalies – indicative of concentrated seepage – were measured in the vicinity of sensor pair 3 near to the downstream toe of the dyke (Rittgers *et al.*, 2014). It is worth noting that softening and localised slope instabilities at the toe were visually observed around $T = 110$ h in the same area.

CONCLUSION

In this work, a novel application of passive seismic interferometry was presented to successfully monitor temporal changes in earthen embankments during internal erosion. Two sets of passive seismic data were analysed. The first one was collected on a canal embankment model tested to failure at the US Bureau of Reclamation of Denver. The noisy environment enabled the reconstruction of seismic impulse responses along the crest of the levee and the monitoring of their change throughout the test. Time-lapse seismic velocity changes associated with induced internal erosion revealed a spatial pattern in agreement with the location of the pipe. Relative velocity decreases of up to 20% were measured, reflecting the stress and porosity redistribution induced by the piping process.

The second dataset was collected on a field-scale levee testing experiment (IJkdijk). Here, the dominant ambient noise source came from discharge flow through a downstream outlet pipe. The signal created by this discharge was sufficient to passively monitor seismic velocities in the structure. The average surface wave velocity decreased by 30% during the significant hydraulic loading period of the embankment and remained relatively stable thereafter. Localised responses from four sensor pairs approximately aligned with the noise source revealed a stronger connection between local seismic velocity and pore water pressure behaviour, including both gradual changes with time and abrupt changes. These responses are consistent with the strong influence of effective stress on surface wave velocity.

This first application of passive seismic interferometry to time lapse internal erosion monitoring in embankments shows great promise for this technique. The ability to remotely monitor changes in meaningful embankment parameters both spatially and with time provides a very valuable tool. That said, the success of the approach is strongly influenced by the presence and nature of the ambient noise sources. A more uniform distribution of ambient noise sources is required to reveal a more comprehensive spatial distribution of seismic velocity changes. New experiments are ongoing on sea levees that are near high-traffic roads, where the breaking waves and the traffic noise are expected to generate more coherent noise for the seismic interferometry technique. Alternatively, active seismic interferometry could be made possible by placing a few automated and continuous sources along levee sections of interest. In these cases, the frequency content and thus wavelengths of the probing signals could be prescribed to image at desired scales.

In terms of imaging resolution, the intrinsic capacities and limitations of the presented method are related to those of active surface wave imaging. The depth sensitivity range is determined by the wavelength of the surface waves, calculated from the ambient noise frequency content and the surface wave velocity along the structure. Assuming ambient noise in the 5–50 Hz range (traffic noise, sea wave action) and surface wave velocities around 100–200 m/s, a depth range from about 2 to 20 m could be investigated. The lateral resolution is related to sensor spacing and wavelength. The diameter of internal erosion channels is likely to be on a scale of 0·1 wavelength or smaller. Thus the complicated patterns followed by individual erosion channels cannot be imaged. However, it is expected that levee sections significantly altered by internal erosion could be detected and located with a resolution of a wavelength (2–20 m).

ACKNOWLEDGEMENTS

The authors acknowledge Tony Wahl and the US Bureau of Reclamation of Denver for granting access to the canal embankment failure experiment. They acknowledge the IJkdijk Foundation (Wouter Zomer) and Andre Koelewijn of Deltares for their assistance during testing and permission to participate. The authors would also like to thank Benjamin Lowry and Jacob Grasmick for their help with the geophysical data acquisition and Wim Kanning for helpful discussions. Funding for this study was provided by the National Science Foundation under the SmartGeo Program (Project IGERT: Intelligent Geosystems; DGE-0801692) and the Partnerships for International Research and Education (PIRE) Program (PIRE: Advancing Earth Dam and Levee Sustainability through Monitoring Science and Condition Assessment; OISE-1243539).

NOTATION

A, n	constants that depend on soil
C_u	coefficient of uniformity
D	damping ratio
e	void ratio
f	frequency
G_0	low-strain shear modulus
I	intensity of seismic wave
I_0	intensity at source location
L_a	attenuation length
$n_A(t)$	ambient noise measured in A in time domain
$n_A(\omega)$	ambient noise measured in A in frequency domain
Q	quality factor

T elapsed time
t_c centre time of time window
v seismic wave group velocity
ΔT time window
δt time delay
λ wavelength
ρ soil density
σ_0' effective mean confining stress
ω angular frequency

REFERENCES

ASCE (American Society of Civil Engineers) (2013). Levees. In *2013 Report card for America's infrastructure*. Reston, VA, USA: American Society of Civil Engineers. See http://www.infrastructurereportcard.org/levees/ (accessed 24/11/2015).

Bakulin, A. & Calvert, R. (2006). The virtual source method: theory and case study. *Geophysics* **71**, No. 4, SI139–SI150.

Bakulin, A., Mateeva, A., Mehta, K., Jorgensen, P., Ferrandis, J., Herhold, I. & Lopez, J. (2007). Virtual source applications to imaging and reservoir monitoring. *The Leading Edge* **26**, No. 6, 732–740.

Behm, M., Leahy, G. M. & Snieder, R. (2014). Retrieval of local surface wave velocities from traffic noise – an example from the La Barge basin (Wyoming). *Geophys. Prospecting* **62**, No. 2, 223–243.

Bensen, G., Ritzwoller, M., Barmin, M., Levshin, A., Lin, F., Moschetti, M., Shapiro, N. & Yang, Y. (2007). Processing seismic ambient noise data to obtain reliable broad-band surface wave dispersion measurements. *Geophys. J. Int.* **169**, No. 3, 1239–1260.

Boué, P., Poli, P., Campillo, M., Pedersen, H., Briand, X. & Roux, P. (2013). Teleseismic correlations of ambient seismic noise for deep global imaging of the earth. *Geophys. J. Int.* **194**, No. 2, 844–848.

Brenguier, F., Campillo, M., Hadziioannou, C., Shapiro, N., Nadeau, R. M. & Larose, E. (2008a). Postseismic relaxation along the San Andreas fault at Parkfield from continuous seismological observations. *Science* **321**, No. 5895, 1478–1481.

Brenguier, F., Shapiro, N. M., Campillo, M., Ferrazzini, V., Duputel, Z., Coutant, O. & Nercessian, A. (2008b). Towards forecasting volcanic eruptions using seismic noise. *Nature Geosci.* **1**, No. 2, 126–130.

Ebrahimian, M., Rahmani, M. & Todorovska, M. I. (2014). Nonparametric estimation of wave dispersion in high-rise buildings by seismic interferometry. *Earthquake Engng Struct. Dynamics* **43**, No. 15, 2361–2375.

Fell, R., Wan, C., Cyganiewicz, J. & Foster, M. (2003). Time for development of internal erosion and piping in embankment dams. *J. Geotech. Geoenviron. Engng* **129**, No. 4, 307–314.

Flood Control IJkdijk (2015). See http://www.floodcontrolijkdijk.nl/en/ (accessed 10/11/2015).

Forghani, F. & Snieder, R. (2010). Underestimation of body waves and feasibility of surface wave reconstruction by seismic interferometry. *The Leading Edge* **29**, No. 7, 790–794.

Foster, M., Fell, R. & Spannagle, M. (2000). The statistics of embankment dam failures and accidents. *Can. Geotech. J.* **37**, No. 5, 1000–1024.

Galetti, E. & Curtis, A. (2012). Generalised receiver functions and seismic interferometry. *Tectonophysics* **532**, 1–26.

Ishihara, K. (1996). *Soil behaviour in earthquake geotechnics*, Oxford Engineering Science Series. Oxford, UK: Clarendon Press.

Kanning, W., Van Baars, S. & Vrijling, J. (2008). The stability of flood defenses on permeable soils: the London avenue canal failures in New Orleans. *Proceedings of the 6th international conference on case histories in geotechnical engineering*, Arlington, VA, USA, No. 2.72.

Lin, F. C., Tsai, V. C., Schmandt, B., Duputel, Z. & Zhan, Z. (2013). Extracting seismic core phases with array interferometry. *Geophys. Res. Lett.* **40**, No. 6, 1049–1053.

Mainsant, G., Larose, E., Brönnimann, C., Jongmans, D., Michoud, C. & Jaboyedoff, M. (2012). Ambient seismic noise monitoring of a clay landslide: toward failure prediction. *J. Geophys. Res.* **117**, No. F1, F01030.

Mooney, M. A., Parekh, M. L., Lowry, B., Rittgers, J. B., Grasmick, J., Koelewijn, A. R., Revil, A. & Zhou, W. (2014). Design and implementation of geophysical monitoring and remote sensing during a full-scale embankment internal erosion test. In *Geo-congress 2014 technical papers: geo-characterization and modeling for sustainability* (eds M. Abu-Farsakh, X. Yu and L. R. Hoyos), Geotechnical Special Publication No. 234, pp. 202–211. Reston, VA, USA: American Society of Civil Engineers.

Nakata, N. & Snieder, R. (2014). Monitoring a building using deconvolution interferometry. II: ambient-vibration analysis. *Bull. Seismol. Soc. Am.* **104**, No. 1, 204–213.

Nakata, N., Snieder, R., Kuroda, S., Ito, S., Aizawa, T. & Kunimi, T. (2013). Monitoring a building using deconvolution interferometry. I: earthquake-data analysis. *Bull. Seismol. Soc. Am.* **103**, No. 3, 1662–1678.

Obermann, A., Planès, T., Larose, E. & Campillo, M. (2013). Imaging preeruptive and coeruptive structural and mechanical changes of a volcano with ambient seismic noise. *J. Geophys. Res.* **118**, No. 12, 6285–6294.

Renalier, F., Jongmans, D., Campillo, M. & Bard, P. Y. (2010). Shear wave velocity imaging of the Avignonet landslide (France) using ambient noise cross correlation. *J. Geophys. Res.* **115**, No. F3, F03032.

Rittgers, J., Revil, A., Planès, T., Mooney, M. & Koelwijn, A. (2014). 4D imaging of seepage in earthen embankments with time-lapse inversion of self-potential data constrained by acoustic emissions localization. *Geophys. J. Int.* **200**, No. 2, 758–772.

Santamarina, J., Klein, K. & Fam, M. (2001). *Soils and waves: particulate materials behavior, characterization and process monitoring*, Lasers and Fibre Optics Series. Hoboken, NJ, USA: J. Wiley & Sons.

Sens-Schönfelder, C. & Wegler, U. (2006). Passive image interferometry and seasonal variations of seismic velocities at Merapi volcano, Indonesia. *Geophys. Res. Lett.* **33**, No. 21, L21302.

Snieder, R. & Larose, E. (2013). Extracting earth's elastic wave response from noise measurements. *Annual Rev. Earth Planetary Sci.* **41**, No. 1, 183–206.

Snieder, R. & Safak, E. (2006). Extracting the building response using seismic interferometry: theory and application to the Millikan Library in Pasadena, California. *Bull. Seismol. Soc. Am.* **96**, No. 2, 586–598.

Van Beek, V., de Bruijn, H., Knoeff, J., Bezuijen, A. & Förster, U. (2010). Levee failure due to piping: a full-scale experiment. *Proceedings of scour and erosion*, San Francisco, CA, USA, pp. 283–292.

Wahl, T. L. & Lentz, D. J. (2012). Experimental methods for studying canal breach processes. *Proceedings of specialty conference on hydraulic measurements and experimental methods*, Snowbird, UT, USA.

Wegler, U. & Sens-Schönfelder, C. (2007). Fault zone monitoring with passive image interferometry. *Geophys. J. Int.* **168**, No. 3, 1029–1033.